# Competing Forces in the Self-Assembly of Coupled ZnO Nanopyramids

Elsa Javon,[†] Meriem Gaceur,[‡] Walid Dachraoui,[‡] Olivier Margeat,[‡] Jörg Ackermann,[*,‡] Maria Ilenia Saba,[§] Pietro Delugas,[§,||] Alessandro Mattoni,[§] Sara Bals,[*,†] and Gustaaf Van Tendeloo[†]

[†]Electron Microscopy for Materials Research (EMAT), University of Antwerp, Groenenborgerlaan 171, 2020 Antwerp, Belgium, [‡]Aix-Marseille Université, CNRS, CINaM UMR 7325, 13288 Marseille, France, [§]Istituto Officina dei Materiali (CNR-IOM) Unità Cagliari SLACS, Cittadella Universitaria, I-09042 Monserrato (CA), Italy, and [||]CompuNet, Istituto Italiano di Tecnologia (IIT), Via Morego 30 16163 Genova, Italy

ABSTRACT Self-assembly (SA) of nanostructures has recently gained increasing interest. A clear understanding of the process is not straightforward since SA of nanoparticles is a complex multiscale phenomenon including different driving forces. Here, we study the SA between aluminum doped ZnO nanopyramids into couples by combining inorganic chemistry and advanced electron microscopy techniques with atomistic simulations. Our results show that the SA of the coupled nanopyramids is controlled first by morphology, as coupling only occurs in the case of pyramids with well-developed facets of the basal planes. The combination of electron microscopy and atomistic modeling reveals that the coupling is further driven by strong ligand—ligand interaction between the bases of the pyramids as dominant force, while screening effects due to Al doping or solvent as well as core—core interaction are only minor contributions. Our combined approach provides a deeper understanding of the complex interplay between the interactions at work in the coupled SA of ZnO nanopyramids.
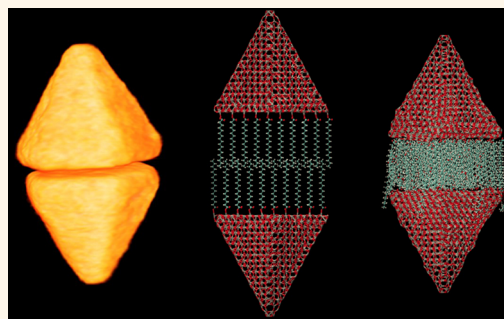
KEYWORDS: self-assembly · dipole—dipole force · ligands · electron tomography · ZnO nanocrystal · model potential molecular dynamics · hybrid nanostructures

Over the past decade, self-assembly (SA) of semiconductor nanocrystals (NCs) into ordered superstructures has gained increasing attention because of their technological applications in nanoscale devices.[1−4] Assembling NCs can generate new collective properties, which are different from single NC yielding new nanostructures with versatile functions.[5,6] A thorough understanding of the SA mechanism of NCs to organize into ordered one- (1D), two- (2D) or three-dimensional (3D) superstructures is thus one of the key topics of future nanoscience.[7] Semiconductor SA is a complex phenomenon that depends on the interplay of several physical factors and competing interactions of different nature. First, the NC shape and size will largely impact the NC assembly.[8] Second, a wide range of interactions plays an important role in SA of NCs including the cohesive forces of the bulk material as well as long-range electrostatic multipole interactions, hydrophobic forces or hydrogen bonding and dispersive van der Waal ones.[5,9−11] Therefore, depending on the NC system,

there is a complex competition that will finally lead to specific SA. Here, we study the mechanism behind SA in zinc oxide (ZnO) NCs that have attracted great attention because of their potential application fields such as solar cells, photocatalysis, UV lasing or chemical sensing.[12−15] In addition to these applications, studying the SA mechanism for ZnO NCs is also of great fundamental importance as this type of particles represents an interesting model system because of their large pallet of shapes and sizes that can be obtained with or without surface ligands. Furthermore, ZnO possesses internal electric fields due to the hexagonal wurtzite structure that generate, together with shape and ligand related forces, a complex parameter space of SA driving forces.[16−18] Previously, ZnO hexagonal pyramids with tail-to-tail pairs or head-to-tail self-assembled chains (the definition of the different ZnO pyramid assemblies is given in Supporting Information through Table S1) were reported.[11,19] By controlling the absence of ligands and the environmental constraints, the authors

could attribute the SA properties to the relative orientation of ZnO NCs dipoles. In an other study, tail-to-tail SA could also be observed for ligand-controlled synthesis of ZnO nanopyramids.[20] Here again, the SA process was found to be the result of opposite polarization of the pyramids yielding an attraction between bases with different charges. The authors proposed that the SA is related to well-developed facets of the basal planes, but mentioned also that a clear explanation for systematic tail-to-tail coupling between two perfect and faceted hexagonal pyramids is still missing.

Recent advances in the field of transmission electron microscopy (TEM) make it possible to obtain two-dimensional (2D) images with a spatial resolution of down to 50 pm.[21] On top of that, 3D imaging, so-called electron tomography, yields important information, particularly on the self-assembly of NC.[3,9,10,22−24] Moreover, it was shown that the combination of aberration corrected TEM and modeling techniques is a very powerful approach to obtain a thorough understanding of the process of SA.[9]

In this work, we apply advanced 2D and 3D techniques, in combination with atomistic simulations to study the SA of ZnO nanopyramids, here considered as a prototype of NC self-assembly. We have focused our attention on the coupling effect, which is especially prominent for particles that yield a pronounced pyramidal shape. Since the 3D aspects are very important for SA, high-angle annular dark-field scanning transmission electron microscopy (HAADF-STEM) is combined with tomography. Other advanced techniques such as aberration corrected high-resolution transmission electron microscopy (HRTEM), energy dispersive X-ray (EDX) mapping, high resolution HAADF-STEM and annular bright-field (ABF)-STEM are used to acquire extra information about the interconnection of the pyramids. In addition, we performed Model Potential Molecular Dynamics (MPMD) simulations of large ZnO pyramids bearing stearic acid molecules as surface ligands on their base.

On the basis of the combination of TEM results and MPMD simulations, we elucidate on the critical role of ligand−ligand forces in the SA stability, suggesting a mechanism in which the long-range electrostatic forces of ZnO pyramids are overcome by molecular forces in the self-assembled coupled pyramids.

RESULTS/DISCUSSION

ZnO nanopyramids have previously been obtained using different synthesis routes.[11,20,25−29] In this study, we choose a synthesis route of ZnO hexagonal nanopyramids following a procedure developed by Zhizhen Ye et al.[30] The work of Zhizhen Ye et al. focused on the effect of the dopant on the shape evolution of ZnO nanoparticles by using several dopants such as Mg, Cd and Ni demonstrating that in addition to altering the atomic composition of the nanocrystals the introduction of specific dopants lead to dramatic changes in the NC morphology. They observed shape modification from nanopyramids to tetrapods and nanowires depending on the molar ratio of dopant precursor in the reagents. Furthermore, Zhizhen Ye et al. showed that pyramidal shaped NCs are obtained without additional dopants, however the shape and size distribution of the obtained pyramidal NCs were irregular and, importantly, no specific SA properties were observed. In our case, we used aluminum acetylacetonate (Al(acac)$_3$) as dopant to produce Al doped ZnO NCs of different shape. The injection of octadecanol at high temperature (200 °C) allowed the formation of the Al-doped ZnO nanopyramids. We found that the Al precursor introduces only small modification in the shape of the NCs compared to the work of Zhizhen Ye et al. as it can be seen in Supporting Information Figures S1. Our syntheses without using Al dopant generate elongated pyramidal NCs with strong variation in size and shape. In contrast, homogeneously shaped and sized nanopyramids were obtained for an Al concentration between 0.3 at. % and 0.75 at. %, whereas higher Al concentrations lead to pyramids but with strong morphological perturbations. This indicates that the role of Al dopant in the control of the NC shape is different to the others dopant such as Mg, Cd and Ni studied by Zhizhen Ye et al. Al doping mainly leads to an improvement in nanopyramid morphology and a narrowing of the size distribution for specific molar ratios. Importantly, we observed a pronounced self-assembled coupling between nanopyramids along their base. The amount of coupled nanopyramids compared to the total amount of NCs depends on the Al doping concentration. Only for Al concentration of 0.3% and 0.75% the coupling was strong, whereas for higher concentrations or dopant free synthesis, the coupling SA is less pronounced or not existing, respectively. An overview image showing the different NCs shapes and their self-assembly into couples is presented in Figure 1a, while Supporting Information Table S2 summaries the observations. It is worth mentioning that Al doping not only modifies the shape and the coupling of the NCs, but also changes the numbers of free carriers inside the ZnO NCs by replacement of Zn^{2+} with Al^{3+} ions.[31,32] The incorporation of the Al ions in the ZnO crystal was demonstrated by EDX mapping on individual tail-to-tail pyramid couples (see Supporting Information Figure S5) for which a homogeneous distribution of Al^{3+} ions inside the nanopyramids was found. The impact of free charge carriers generated via Al doping on the optical properties of ZnO can be studied from fluorescence spectroscopy. The green emission of ZnO centered at 500 nm is generally caused by intrinsic defects such as oxygen vacancies and zinc interstitials.[33] The fluorescence spectra presented in Supporting Information Figure S2 show that the emission of the defect band decreases with
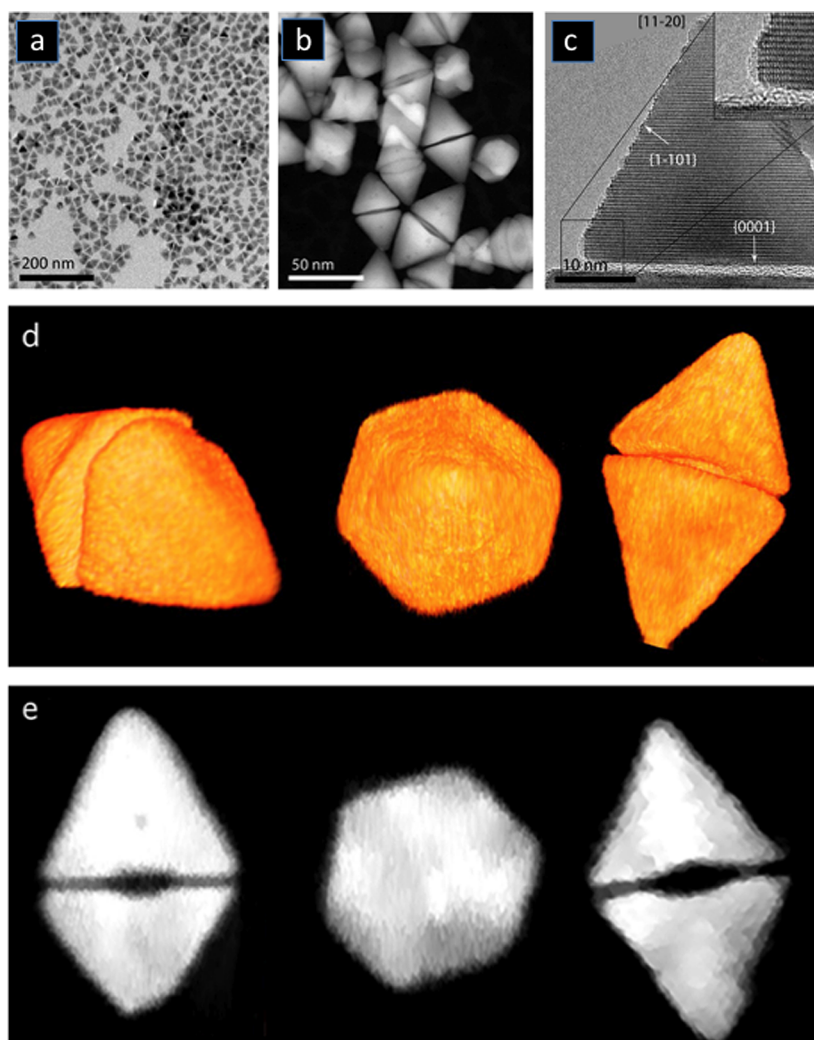
Figure 1. (a) Conventional bright-field TEM overview revealing the systematic coupling of ZnO nanopyramids. (b) HAADF-STEM overview of the coupled ZnO nanopyramids. (c) HR-TEM image of a coupled ZnO nanopyramid viewed along the [11$\bar{2}$0] zone axis. The enlarged part highlights the presence of organic ligands between the bases. (d) Volume rendering of the 3D reconstruction presented along different viewing directions. (e) Three mutually perpendicular slices through the 3D reconstructions.

increasing Al doping. The reduction of the defect emission can be attributed to the suppression of the intrinsic defects by the inclusion of the Al ions in the ZnO crystal.[34] The evolution of the defect peak with Al concentration indicates thus an increased amount of Al ions in the ZnO crystal. Thus, we could show that Al doping not only impacts directly the shapes and sizes of the NCs, but also changes the electronic properties of the NC in terms of amount of free charge carriers inside the NC.[31] Free charge carriers can introduce screening effects during SA processes and has therefore to be considered for understanding the SA properties of the ZnO nanopyramids. We can already state at this point that pronounced SA of ZnO NCs mainly occurs for intermediate doping levels, for which the nanopyramids are homogeneous in shape and size pointing out the dominant role of the ZnO NC morphology. A deeper analysis on possible screening effects induced by free charges and

their impact on ZnO NCs SA is discussed in later section of this work.

Another important question is whether the coupling occurs already in solution or at the moment when NCs are deposited onto carbon grids for TEM investigations. To answer this question, TEM analyses were performed by using graphene liquid cells.[35,36] As illustrated in Supporting Information Figure S3, these analyses show that coupling of nanopyramids is already present in solution.

To understand the origin of the SA in detail, we applied HAADF-STEM to ZnO nanopyramids with 0.75% Al, a preparation that showed the highest degree of tail-to-tail coupling. The HAADF-STEM image in Figure 1b shows nanopyramids yielding a quasi-equilateral triangular shape and an average size between 30 and 40 nm. A systematic coupling is observed although the pyramids are not in direct contact. The HRTEM image shown in Figure 1c demonstrates that

the base of the pyramids is parallel to the {0001} planes and perpendicular to the [0001] *c*-axis corresponding to a common growth direction of the ZnO NCs. The edges are parallel to the {1$\bar{1}$01} planes. The viewing axis corresponds to the [11$\bar{2}$0] direction of the wurtzite structure for at least one of the pyramids in the pairs (more details about the crystallographic relation are available in Supporting Information Figure S4). As demonstrated in the inset of Figure 1c, the lateral facets of the nanopyramids are sharp but show elementary steps on an atomic scale; the base of the pyramids however is atomically flat. As organic ligands such as stearates are released during the synthesis of the ZnO NCs, it is to be expected that they are present at the surface of the pyramids.[30] High resolution TEM (HR-TEM) does not show an organic layer at the side facets, however the basal planes are connected through a thin (1.5−2 nm thick) layer. EDX mapping on individual tail-to-tail pyramid couples was performed and produces a high carbon signal between the pyramids (see Supporting Information Figure S5). Therefore, we conclude that the layer most probably consists of organic ligands still present between the two pyramids after the synthesis. This suggests that the coupling process might be influenced by ligands that are only localized on the well-developed facets of the basal plane, *i.e.* the (0001) surfaces. Given the organic nature of the layer, it is not possible to obtain further information on their detailed structure by TEM. As mentioned, we only observed these ligands at high concentration between the bases of the coupled pyramids whereas lateral surfaces are almost ligand free. The selective interaction with basal planes could be attributed to its polar nature providing additional attractive forces with carboxylic groups. Taking into account that the stearate concentration is very high during synthesis and that a ligand monolayer should be generated all over the surface due to the efficient grafting of stearates to the ZnO surface, we can expect that they are present on all faces during synthesis. As postsynthesis washing steps were used before TEM analysis, it is therefore reasonable to think that most ligands are removed during washing steps. The fact that intercalated ligand monolayers between the bases of the coupled pyramids have not been affected by the washing steps indicate their high stability. This goes in line with our observation that redispersion of the washed samples in different solvents (see Supporting Information) could not disassemble the nanopyramid couples.

To confirm the hexagonal pyramid morphology and entirely characterize the 3D shape of the strongly faceted and coupled nanopyramids, electron tomography was applied. Therefore, a tilt series of 2D HAADF-STEM images was acquired, aligned and combined through a mathematical algorithm. HAADF-STEM images acquired at different tilt angles are presented

in the Supporting Information (Figure S6). The result of the 3D reconstruction is illustrated in Figure 1d through a volume rendering. Faceting of the pyramids is well highlighted by this 3D visualization and provides direct proof for the different morphological models that were suggested using different techniques in earlier studies.[11,17,29] A random rotation of the bases is observed for each couple through the electron tomography reconstruction. Some pairs are well aligned whereas others are misaligned such that corners of one of the hexagonal base correspond to edges of the other one. Figure 1e shows 3 perpendicular slices through the reconstruction. These cross sections confirm the pyramidal morphology and show that the base of the pyramids is very close to a regular hexagon, although slightly distorted in some of the pyramid couples. The symmetry that is observed between the top and bottom of the coupled structure proves that attached pyramids have a quasi-identical morphology. The orthoslices also suggest that dimples are present at the bottom of the pyramids. However, despite of the systematic presence of the dimples in their center, the basal planes appear very flat and parallel within each couple.

To better understand the coupling process, high resolution HAADF-STEM images of the connecting area between the pyramids are acquired (Figure 2a). It seems that despite some misalignment of the pyramids, the *c*-axis of the top one exactly coincides with the *c*-axis of the bottom one. The HAADF-STEM image was acquired such that the atomic columns of the bottom pyramid are oriented along the [11$\bar{2}$0] zone axis. At the same time, the (0001) planes of the upper pyramid can be observed. Since the {0001} planes can be observed in both pyramids it is confirmed that they are accurately parallel and perpendicular to a common *c*-axis. This means that the misalignment between the pyramids corresponds to a rotation around their common *c*-axis. The results indicate that the SA process is independent of possible alignment of ZnO NC bases and allows for rotational freedom around the *c*-axis.

In earlier studies,[20] the coupling of the nanopyramids was attributed to the intrinsic polarity along the [0001] direction of the ZnO nanoparticles. Indeed, ZnO is a wurtzite-type crystal that can be described as a number of alternating planes composed of 4-fold tetrahedrally coordinated O^{2-} and Zn^{2+} ions stacked alternatively along the *c*-axis. One face of the hexagonal sheet is Zn rich and forms the (0001) planes whereas the opposite face is O rich and forms the (000$\bar{1}$) planes. Thus, the ZnO crystals are polar in nature along the [0001] axis. The orientation of the O-(000$\bar{1}$) and Zn-(0001) planes relatively to the *c*-axis determines whether the tip of the nanopyramid structure points toward the [0001] or the [000$\bar{1}$] direction. This feature is of high importance since it defines the polarization of the pyramids and would lead to a
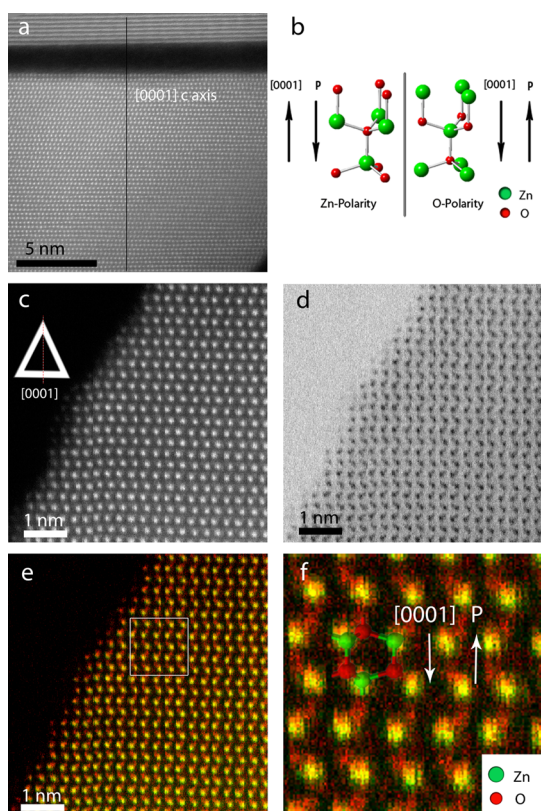
Figure 2. (a) HAADF-STEM images of the contact area of a couple of nanopyramids. The bottom pyramids is oriented along the [11$\bar{2}$0] zone axis and the top one is only in an orientation perpendicular to the *c*-axis. (b) Definition of the polarization for the ZnO wurtzite structure: Zn-polarity (left) and O-polarity (right). (c) Atomic resolution aberration corrected HAADF-STEM detail of the ZnO wurtzite structure in a zoomed-in region of the edge of the nanopyramid. (d) Atomic resolution aberration corrected ABF-STEM detail from the same area as in (c). (e) Temperature colored detail of the HAADF-STEM image (green colored) superimposed with the ABF-STEM image (red colored) of the same region. (f) Magnified detail of (e), superimposed with the schematic wurtzite atomic structure (Zn atoms in green and O atoms in red).

preferential coupling of bases with different polarization. It is therefore important to study the polarity of the nanopyramids. In addition, the termination of the exposed polar-surfaces {10$\bar{1}$1} and {0001} will play a very different role when binding to ligand molecules.[17] In the Supporting Information, atomic models show the most stable atomic layers terminating the edges and the base of the pyramids (Supporting Information Figure S7).

Different methods exist to determine the polarity: due to the noncentrosymmetry of the wurtzite structure, convergent beam electron diffraction (CBED)[29,37] or selected area electron diffraction (SAED) by tilting around the [0001] direction can be used.[17] Electron holography is also useful to map the localized charges in the surfaces induced by the polarization.[16] Recently, the termination of wurtzite rod-shaped ZnSe/ZnS core/shell nanoparticles was determined by the exit wave reconstructions and verified by HAADF-STEM images.[38]

Here, we used a relatively novel method combining HAADF-STEM and annular bright-field (ABF)-STEM imaging, which allows mapping of lightest elements.[39] This technique was successfully used in earlier studies to determine the polarization of ZnO and GaN-AlN nanowires.[40]

In Figure 2, HAADF-STEM (c) and ABF-STEM (d) images, simultaneously acquired, are depicted. By inverting the contrast of the ABF-STEM image and superimposing it to the HAADF-STEM image with a respectively red and green color map, we are able to visualize Zn and O atomic columns along the [11$\bar{2}$0] zone axis (Figure 2e,f). In Figure 2f, the orientations of the Zn–O dumbbells corresponding to a specific polarization are clear. Since O-planes correspond to the (000$\bar{1}$) surfaces and Zn planes to the (0001) surfaces, the orientation of the dumbbell relatively to the *c*-axis gives the direction of the polarity of the nanopyramid. Here, the Zn atom is oriented toward the base and O points toward the tip that corresponds to the O-polarization according to the definition of the polarity (Figure 2b). Since it is highly unlikely that the last (0001) plane terminating the base of the pyramid would correspond to half a Zn–O dumbell, it can be expected that the base of the pyramid is Zn-terminated. The corresponding model is presented in the Supporting Information (Figure S7a,b). A similar approach was applied to four other pyramids, and the same unique O-polarization was found (see Supporting Information S7c,d). This strongly suggests that the nanopyramids in a couple are facing each other with the same polarity. This is an important result since apparently the tail-to-tail assembly of ZnO pyramids occurs in the presence of repulsive forces induced by the opposite polarization in coupled pyramids. Interestingly, such tail-to-tail assembly of ZnO nanopyramids with the same polarity could be observed by Kotov *et al.*[7,11] but only by using excluded volume interactions of a polymer additive, while in our study, the situation is completely different as ligands are found to be present at the surface of the NCs. In conclusion, our advanced electron microscopy techniques could reveal first that ligands are present only between the bases of coupled nanopyramids and may be responsible for the SA process. Furthermore, the SA process occurs with freedom of rotation around the *c*-axis along and, more importantly, in the presence of identical polarization of the coupled NCs.

To understand the origin of SA process of the Al doped ZnO nanopyramids, we have to consider several parameters. Considering first the dimples in the center of the basal planes, it is possible that it is at the origin of the SA as it could be indicative for the presence of a seed from which both pyramids grow in an opposite direction. The presence of such dimples at the base of twinned NCs was so far observed in the cases of twinned ZnO pyramids.[41] Furthermore, Xuefei *et al.*
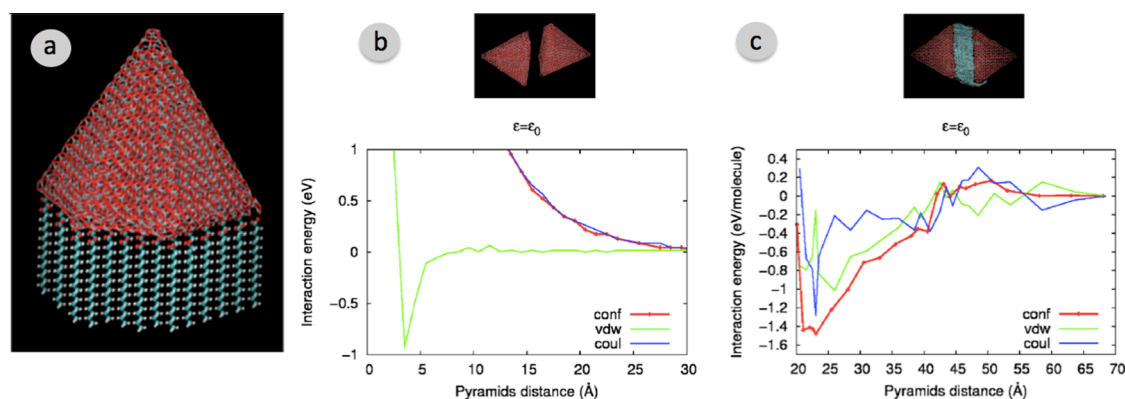
Figure 3. (a) Model of ZnO pyramid with a stearic acid layer covering the Zn terminated basis. Energy of two ZnO pyramids as a function of their distance, without (b) and in the presence of stearic acid (c). The total configurational energy (red line) is the sum of dispersive (vdw, green) and electrostatic (coul, blue line) contributions.

observed coupling of ZnO cones *via* the growth of nanocones with a dimple at the base from which a second nanocone started to grow.[42] In both cases, so synthesized twinned ZnO NCs were of micrometer size, for which SA driven forces can be considered differently from those at nanoscale. To see whether the presence of the dimples is related to the SA of the nanopyramids in this work, we monitored the growth of the NCs by TEM on aliquots from the reaction solution at different times. As shown in Supporting Information Figure S8, one can see that shape and size of the NCs changes with growth time, but only well shaped nanopyramids form coupling *via* SA with increasing growth time. Thus, we can exclude a growth mechanism based on a nucleation seed or a process similar to the work of Xuefei *et al.* to be responsible for the observed pyramid coupling. The dimples observed here in the case of ZnO nanopyramids are thus not a dominant parameter in the SA process. As these TEM analyses have been performed with samples taken from the synthesis solution, *i.e.*, without postsynthesis washing steps, it demonstrates further that the twinning occurs already during the synthesis and not during the washing steps.

The question arises now whether surface ligands that were observed at high concentration between the bases of the coupled pyramids are able to introduce attractive forces between the NCs that enable to overcome the long-range repulsive electrostatic forces of ZnO pyramids. Furthermore, we mentioned earlier that Al doping of the ZnO NC not only changes the morphology of the NCs but also generates free charge carriers inside the pyramids. Thus, the role of Al doping in the SA process in terms of screening of the electrostatic repulsive has to be considered. As the SA is observed already in solution it is also of importance to take into account solvent effects that are able to generate screening effects.

To clarify the role of the different parameters involved in the coupling of the pyramids, we performed Model Potential Molecular Dynamics (MPMD) simulations

of ZnO pyramids bearing stearic acid molecules as surface ligands on the base. Therefore, we generated models of hexagonal ZnO pyramids (the smallest model contained >4000 atoms) with Zn terminated (0001)-bases and six ($1\bar{1}01$) lateral surfaces consistent with the experimental indications. The atomistic models of the pyramids are illustrated in Figure 3a (Zn atoms are gray and O are red). By choice, we considered first undoped neutral pyramids obtained by replicating Zn^{2+}/O^{2-} dimers and cutting along the proper crystallographic planes. Charge neutrality implies that Zn and O terminated lateral facets alternate around the pyramid. The interatomic forces were calculated according to a two-body Buckingham potential that includes long-range electrostatic Coulomb interactions. The ligand molecules (see Figure 3a) were modeled within an AMBER type potential and they interact with the pyramid through van der Waals and electrostatic forces between atomic partial charges (see Methods for more details), thus bonding, dispersive, electrostatic and, in particular, the core—core dispersive contribution were included in the model. An efficient bidentate anchoring mechanism has been found for the deprotonated carboxyl group of the stearic acid and the Zn atoms of the surface (consistent with literature).[43] The density of ligand molecules on the Zn basis was chosen approximately as one chain per two adsorption sites corresponding to a molecule—molecule distance within the organic film of ∼0.6 nm (Figure 3a). This value is close to the calculated optimal distance between the molecules that minimizes the energy of an ordered freestanding monolayer of parallel stearic acid chains (∼0.67 nm).

To study the SA process, we first considered the interaction between two pyramids in the absence of any ligands (Figure 3b). It is shown that the total pyramid—pyramid interaction is repulsive at any distance (red curve) due to the strong electrostatic repulsion (blue curve) that largely dominates the very weak core—core dispersive forces at shorter distances (green curve). Accordingly, in order to have attraction, it is

mandatory to sizably reduce the coulomb term. By introducing the ligands on the planes of the pyramides as shown in Figure 3c, we found that their presence enables the occurrence of a stable bound system, in which the two pyramids are aligned and the stearate molecules form an ordered interdigitated organic film in between. The pyramids attract each other until they reach the minimum energy distance corresponding approximately to the ligand film thickness. The attraction is mainly due to the ligand−ligand interactions within the two interdigitated organic layers for which the calculated equilibrium distance is slightly longer than the experimental one. This discrepancy can be attributed to different factors that are not considered in our model and that can reduce the order of the polymeric film and allow the tilt of the molecules such as disorder, temperature, different density of the ligands, or surface defects.

By starting from the bound state, we calculate the total configurational energy (red line) per pyramid dimer (see Figure 3c) as a function of the pyramid distance. The two pyramids were rigidly separated and for each distance, the corresponding energy was calculated after a local atomic relaxation. A strong minimum energy (1.48 eV/mol) is found at around 2−2.5 nm distance, consistent to the tight binding of the two pyramids that vanishes at distances larger than 4 nm. Thus, an overall energy gain of ∼1.7 eV/molecule is obtained during the SA process and is need to be overcome to disassemble the system.

As a next step, we calculated the effect of free charges in the SA process. As shown earlier, free charge carriers are generated during the Al doping inside the ZnO NCs filling up existing defect states inside the ZnO and competing with already existing free charge carriers due to oxygen vacancies inside the NCs. It is likely that the free charges will tend to redistribute in order to screen the effective atomic charges of the ions. This lowers the electrostatic repulsion between the pyramids and favors the assembling. To demonstrate quantitatively this effect, we considered first the effect of screening on the interaction between two pyramids in vacuo (Supporting Information Figure S9, left panel) and without ligands (Supporting Information Figure S9, right panel). The screening is obtained by rescaling of the charges by a factor $\alpha > 1$ (in Supporting Information Figure S9 we reported the case $\alpha = 5$). It is found that under sufficiently strong screening conditions the total pyramid−pyramid repulsion is lowered and the interaction becomes attractive due to dispersive core−core attraction. This shows that this screening is favorable for assembling. However, the stabilizing dispersive core−core forces are much weaker with respect to the case of ligands. More importantly it would induce a distance between the twinned ZnO NCs as small as 0.3 nm, which is in discordance with a much longer 1.5−2 nm separation expected in the case of ligands and observed experimentally.

We also considered the effect of a change of the dielectric constant on the interaction of pyramids. In this way we can take into account the role of solvent whose dielectric constant is typically different from one. In absence of ligands the effect of the dielectric function on the interaction is totally equivalent to the screening of ZnO charges already discussed (Supporting Information Figure.S2, b) considering that, in the electrostatic interaction ($\sim q^2/4\pi\varepsilon_0$) the charge rescaling ($q \rightarrow q/\alpha$) is equivalent to increase the dielectric function by a factor $\varepsilon_r = \alpha^2$. In presence of ligands, an additional calculation is necessary. The case $\varepsilon_r = 1$ (vacuo) corresponds to the data show in Figure 3c. The total attractive interaction (red curve) is due to the ligands that are able to screen the coulomb term (blue line) and provides a large dispersive attraction (green). The case of larger dielectric constant is reported in the right panel of Supporting Information Figure S10 for $\varepsilon_r = 4$ (representative for the solvents used for of SA observation). The coulomb term is lowered by the dielectric constant but there is still a remaining attractive total configurational energy per pyramid dimer (∼1 eV/molecule) mainly due to dispersive interligand forces. Thus, we can conclude that the crucial force counteracting the SA process is the electrostatic repulsion between the Zn-terminated cores, which can be strongly reduced by the presence of free charges inside the NC as well as by the solvent, both making the occurrence of SA process easier. Interestingly, our simulations show that there could be an initial small energy barrier during the process of ligand intercalation of initially separate pyramids as seen in Figure 3c. Since the synthesis of the ZnO pyramids takes place at elevated temperature, it is likely that this barrier is easily overcome thermally during the synthesis. We also can assume from our calculations that solvent or charge screening effects reduces this barrier as shown in Supporting Information Figure S10. To summarize, our simulations reveal that the essential driving force accounting for the SA process of the nanopyramids comes from the ligand−ligand interaction between the bases of the nanopyramids that governs the SA process even in absence of solvent or charge screening

CONCLUSION

In conclusion, by combining inorganic chemistry with state-of-the art advanced scanning transmission electron microscopy and electron tomography with Model Potential Molecular Dynamics simulations, we were able to obtain deeper insight in the nature of the forces and their balance generating a tail-to-tail SA of ZnO pyramids. From the synthetic side, we used Al doping to finely tune the shape of the ZnO NCs and found clear evidence that the SA of ZnO NCs is directly related to their morphology. Only in the case of well-developed nanopyramids with atomically flat bases,

we observed a pronounced self-assembly into a tail-to-tail configuration. From HAADF-STEM analyses, we conclude that tail-to-tail SA of ZnO pyramids occurs even in the presence of repulsing forces induced by the opposite polarization in coupled pyramids. The Model Potential Molecular Dynamics simulations considered different parameters such as ligand forces, screening effects arising from either free charges due to Al doping of ZnO or from solvents. Our results reveal that the essential parameter that controls the SA process of the nanopyramides is the interactions between the ligands.

A tail-to-tail assembly is not likely to occur in the absence of ligands. Thus, we obtain clear indications that stearate monolayers at the base of the pyramids introduce attractive forces between the pyramids, allowing overcoming long-range electrostatic forces between the pyramid dipoles and efficiently binding the pyramids into a tail-to-tail configuration. This work highlights the powerful combination of complementary techniques in order to investigate the complex interplay of material, morphology and ligand related driving forces leading to self-assembly of nanocrystals.

METHODS

Synthesis of ZnO Nanopyramids. Zinc stearate (Zn(St)$_2$), 1-octadecanol (ODA, 97%) and 1-octadecene (ODE, tech 90%) were purchased from Alfa Aesar. Aluminum acetylacetonate (Al(acac)$_3$) was purchased from Sigma-Aldrich. All chemicals were used without further purification. The molar ratios of Al(acac)$_3$:Zn(St)$_2$ were varied to adjust the final composition: 0:100 (pure ZnO), 3:97 (0.32% doped), 5:95 (0.75% doped), and 20:80 (1.2% doped). The ZnO NCs were synthesized following a procedure developed by Zhizhen Ye et al.[30] who used Mg, Cd and Ni dopant. The synthesis is adapted here with a choice of an appropriate aluminum precursor as doping agent to improve the pyramidal morphology in order to get the SA. In a typical procedure for preparing ZnO nanocrystals (0.75% doped), 0.95 mmol of Zn(St)$_2$, 0.05 mmol of Al(acac)$_3$ and 20g of ODE were loaded in 100 mL three-necked flask, degassed and heated up to 270 °C under an argon flow. A separate solution containing 5g of ODE and 5 mmol of ODA at 200 °C was rapidly injected into the reaction flask under vigorous magnetic stirring. The formation of the NCs is immediate but the reaction temperature, which dropped down to 245 °C due to the injection, was allowed to rise to 270 °C by heating in 6 min and stabilized afterward. Once this temperature was reached, the mixture was kept at this temperature for additional 60 min and then cooled to room temperature in ambient conditions. Next, 40 mL of ethyl acetate was added to the reaction mixture in order to precipitate the ZnO NCs from the solution. The NCs were collected by centrifugation, followed by three washing steps using toluene and methanol. The obtained surfactant-coated ZnO NCs were able to be redispersed in organic solvents such as ODA, ODE, heptane, toluene or chloroform for characterization. In all cases, nanopyramid twinning SA was observed for 0.32% Al-doped and 0.75% Al-doped nanopyramids, i.e., for the NCs having near perfect pyramidal shapes.

Transmission Electron Microscopy. Dilute solutions of the particles in toluene were drop-casted onto a carbon-coated copper TEM grid. Conventional bright-field TEM images were taken using a FEI Tecnai F-20. Tilt series for tomography were acquired in HAADF-STEM. Similar samples were placed in a Fischione ultrahigh tilt tomography holder (model 2020) and inserted into the same microscope operated at 200 kV. Image acquisition was performed manually with an acquisition time of 10 s per image. Images were acquired over an angular range of −72° to +74° with a tilt increment of 2°. This tilt series was aligned using inspect3D. Reconstructions were performed using either the iterative routine (SIRT) as implemented in inspect3D or by applying the total variation minimization technique (TVM) with a developed scripting based on compressive sensing.[58] 3D visualizations were carried out using the Amira software. The EDX maps were acquired with a chemiSTEM detector. Aberration corrected STEM experiments were performed using a FEI TITAN "cubed" 80−300 transmission electron microscope operated at 300 kV. The convergence semiangle was 21 mrad, the acceptance semiangle for HAADF-STEM was 41.5 mrad and the angular range for the ABF images was 7.5−25.7 mrad.

Simulations. All the atomistic models were generated by model potential molecular dynamics simulations by using the DL_POLY_4 code[44] and analyzed by using the VMD molecular visualization program.[45] The velocity-Verlet algorithm[46] with a time step as small as 0.5 fs was used to solve the equations of motion.

The minimum energy configuration of the bound pyramids was obtained by low temperature annealing (∼100 ps) plus atomic forces relaxations based on standard conjugated gradients algorithm.[47]

The stearic acid was modeled by the AMBER force field[48] with AM1-BCC[49] atomic partial charges. Atomic forces within ZnO atoms consisted of Coulomb terms and Buckingham-type two-body potential[50,51] while hybrid organic−inorganic interactions were described as the sum of Coulomb and Lennard-Jones contributions. The Long-range electrostatic forces were calculated by a mesh Ewald algorithm[52] and van der Waals interactions were cutoff at 9.5 Å. The same theoretical scheme has been widely applied in several hybrid nanosystems.[53−57]

Conflict of Interest: The authors declare no competing financial interest.

Supporting Information Available: Definition of the 2D projection corresponding to different organizations, influence of Al-doping on ZnO NC shape, Fluorescence spectra of ZnO NCs as a function of Aluminum doping, NC coupling in solution, Crystallographic indexation of the pyramids, EDX mapping studying presence of ligands, atomic model considering polarity, TEM analysis from aliquots of the reaction solution of 0.75% Al-doped ZnO nanopyramides as a function a time, simulation of pyramid−pyramid (core−core) interaction in absence of ligands *in vacuo* or in the case of ZnO screening, simulation of pyramid−pyramid (core−core) interaction in the presence of ligands *in vacuo*, $\varepsilon_r = 1$ (or in a dielectric medium with $\varepsilon_r = 4$). This material is available free of charge *via* the Internet at http://pubs.acs.org.

REFERENCES AND NOTES

1. Pietra, F.; Rabouw, F. T.; Evers, W. H.; Byelov, D. V.; Petukhov, A. V.; Donega, C. D.; Vanmaekelbergh, D. Semiconductor Nanorod Self-Assembly at the Liquid/Air Interface Studied by in Situ GISAXS and ex Situ TEM. *Nano Lett.* **2012**, *12*, 5515–5523.
2. Evers, W. H.; Goris, B.; Bals, S.; Casavola, M.; de Graaf, J.; van Roij, R.; Dijkstra, M.; Vanmaekelbergh, D. Low-Dimensional

Semiconductor Superlattices Formed by Geometric Control Over Nanocrystal Attachment. *Nano Lett.* **2013**, *13*, 2317–2323.

3. Evers, W. H.; De Nijs, B.; Filion, L.; Castillo, S.; Dijkstra, M.; Vanmaekelbergh, D. Entropy-Driven Formation of Binary Semiconductor-Nanocrystal Superlattices. *Nano Lett.* **2010**, *10*, 4235–4241.

4. Gordon, T. R.; Paik, T.; Klein, D. R.; Naik, G. V.; Caglayan, H.; Boltasseva, A.; Murray, C. B. Shape-Dependent Plasmonic Response aAnd Directed Self-Assembly in a New Semiconductor Building Block, Indium-Doped Cadmium Oxide (ICO). *Nano Lett.* **2013**, *13*, 2857–2863.

5. Grzelczak, M.; Vermant, J.; Furst, E. M.; Liz-Marzan, L. M. Directed Self-Assembly of Nanoparticles. *ACS Nano* **2010**, *4*, 3591–3605.

6. Kinge, S.; Crego-Calama, M.; Reinhoudt, D. N. Self-Assembling Nanoparticles at Surfaces and Interfaces. *ChemPhysChem* **2008**, *9*, 20–42.

7. Tang, Z. Y.; Kotov, N. A. One Dimensional Assemblies of Nanoparticles: Preparation, Properties, and Promise. *Adv. Mater.* **2005**, *17*, 951–962.

8. Jana, N. R. Shape Effect in Nanoparticle Self-Assembly. *Angew. Chem., Int. Ed.* **2004**, *43*, 1536–1540.

9. Galvan-Moya, J. E.; Altantzis, T.; Nelissen, K.; Peeters, F. M.; Grzelczak, M.; Liz-Marzan, L. M.; Bals, S.; Van Tendeloo, G. Self-Organisation of Highly Symmetric Nanoassemblies: A Matter Of Competition. *ACS Nano* **2014**, *8*, 3869–3875.

10. Sanchez-Iglesias, A.; Grzelczak, M.; Altantzis, T.; Goris, B.; Perez-Juste, J.; Bals, S.; Van Tendeloo, G.; Donaldson, S. H.; Chmelka, B. F.; Israelachvili, J. N.; Liz-Marzan, L. M. Hydrophobic Interactions Modulate Self-assembly of Nanoparticles. *ACS Nano* **2012**, *6*, 11059–11065.

11. Yang, M.; Sun, K.; Kotov, N. A. Formation and Assembly-Disassembly Processes of ZnO Hexagonal Pyramids Driven by Dipolar and Excluded Volume Interactions. *J. Am. Chem. Soc.* **2010**, *132*, 1860–1872.

12. McLaren, A.; Valdes-Solis, T.; Li, G.; Tsang, S. C. Shape and Size Effects of Zno Nanocrystals Oon Photocatalytic Activity. *J. Am. Chem. Soc.* **2009**, *131*, 12540–12541.

13. Look, D. C. Recent Advances in Zno Materials and Devices. *Mater. Sci. Eng., B* **2001**, *80*, 383–387.

14. Gurlo, A. Nanosensors: Towards Morphological Control of Gas Sensing Activity. Sno_2, In_2O_3, Zno And WO_3 Case Studies. *Nanoscale* **2011**, *3*, 154–165.

15. Ahmad, M. Z.; Chang, J.; Ahmad, M. S.; Waclawik, E. R.; Wlodarski, W. Non-Aqueous Synthesis of Hexagonal Zno Nanopyramids: Gas Sensing Properties. *Sens. Actuators, B* **2013**, *177*, 286–294.

16. Liu, Y. Z.; Han, X. D.; Zhang, Z. Potential Mapping of ZnO by Off-Axis Electron Holography. *Philos. Mag. Lett.* **2007**, *87*, 103–111.

17. Chang, J.; Ahmed, R.; Wang, H. D.; Liu, H. W.; Lo, R. Z.; Wang, P.; Waclawikt, E. R. ZnO Nanocones with High-Index $\{10\bar{1}1\}$ Facets for Enhanced Energy Conversion Efficiency of Dye-Sensitized Solar Cells. *J. Phys. Chem. C* **2013**, *117*, 13836–13844.

18. Pacholski, C.; K, A.; Weller, H. Self-Assembly of ZnO: From Nanodots to Nanorods. *Angew. Chem., Int. Ed.* **2002**, *41*, 1188–1191.

19. Bell, N. S.; Tallant, D. R.; Raymond, R.; Boyle, T. J. Synthesis and Self-Assembly of Zinc Oxide Nanoparticles with Septahedral Morphology. *J. Mater. Res.* **2008**, *23*, 529–535.

20. Chen, Y.; Kim, M.; Lian, G.; Johnson, M. B.; Peng, X. Side Reactions in Controlling the Quality, Yield, and Stability of High Quality Colloidal Nanocrystals. *J. Am. Chem. Soc.* **2005**, *127*, 13331–13337.

21. Van Tendeloo, G.; Bals, S.; Van Aert, S.; Verbeeck, J.; Van Dyck, D. Advanced Microscopy for Advanced Materials. *Adv. Mater.* **2012**, *24*, 5655–5675.

22. Altantzis, T.; Goris, B.; Sanchez-Iglesias, A.; Grzelczak, M.; Liz-Marzan, L. M.; Bals, S. Quantitative Structure Determination of Large Three Dimensional Nanoparticle Assemblies. *Part. Part. Syst. Charact.* **2013**, *30*, 84–88.

23. Boneschanscher, M. P.; Evers, W. H.; Geuchies, J. J.; Altantzis, T.; Goris, B.; Rabouw, F. T.; van Rossum, S. A. P.; van der Zant, H. S. J.; Siebbeles, L. D. A.; van Tendeloo, G.; Swart, I.; Hilhorst, J.; Petukhov, A. V.; Bals, S.; Vanmaekelbergh, D. Long-Range Orientation and Atomic Attachment of Nanocrystals in 2D Honeycomb Superlattices. *Science* **2014**, *20*, 1377–1380.

24. Friedrich, H.; Gommes, C. J.; Overgaag, K.; Meeldijk, J. D.; Evers, W. H.; de Nijs, B.; Boneschanscher, M. P.; de Jongh, P. E.; Verkleij, A. J.; de Jong, K. P.; van Blaaderen, A.; Vanmaekelbergh, D. Quantitative Structural Analysis of Binary Nanocrystal Superlattices by Electron Tomography. *Nano Lett.* **2009**, *9*, 2719–2724.

25. Herring, N. P.; AbouZeid, K.; Mohamed, M. B.; Pinsk, J.; El-Shall, M. S. Formation Mechanisms of Gold-Zinc Oxide Hexgonal Nanopyramids by Heterogeneous Nucleation using Microwave Synthesis. *Langmuir* **2011**, *27*, 15146–15154.

26. Herring, N. P.; Almahoudi, S. H.; Olson, C. R.; El-Shall, M. S. Enhanced Photocatalytic Activity of ZnO−Graphene Nanocomposites Prepared by Microwave Synthesis. *J. Nanopart. Res.* **2012**, *14*, 1–13.

27. Li, P.; Wang, D. S.; Wei, Z.; Peng, Q.; Li, Y. D. Systematic Synthesis of ZnO Nanostructures. *Chem.—Eur. J.* **2013**, *19*, 3735–3740.

28. Salavati-Niasari, M.; Mir, N.; Davar, F. Zno Nanotriangles: Synthesis, Characterization and Optical Properties. *J. Alloys Compd.* **2009**, *476*, 908–912.

29. Zhou, X.; Xie, Z. X.; Jiang, Z. Y.; Kuang, Q.; Zhang, S. H.; Xu, T.; Huang, R. B.; Zheng, L. S. Formation of ZnO Hexagonal Micro-Pyramids: A Successful Control of the Exposed Polar Surfaces with the Assistance of an Ionic Liquid. *Chem. Commun.* **2005**, 5572–5574.

30. Yang, Y.; Jin, Y.; He, H.; Wang, O.; Tu, Y.; Lu, H.; Ye, Z. Dopant-Induced Shape Evolution of Colloidal Nanocrystals: The Case of Zinc Oxide. *J. Am. Chem. Soc.* **2010**, *132*, 13381–13394.

31. Buonsanti, R.; Llordes, A.; Aloni, S.; Helms, B. A.; Milliron, D. J. Tunable Infrared Absorption and Visible Transparency of Colloidal Aluminum-Doped Zinc Oxide Nanocrystals. *Nano Lett.* **2011**, *11*, 4706–4710.

32. Hammer, M. S.; Rauh, D.; Lorrmann, V.; Deibel, C.; Dyakonov, V. Effect of Doping- and Field-Induced Charge Carrier Density on the Electron Transport in Nanocrystalline ZnO. *Nanotechnology* **2008**, *48*, 48570.

33. Vanheusden, K.; Warren, W. L.; Seager, C. H.; Tallant, D. R.; Voigt, J. A.; Gnade, B. E. Mechanisms Behind Green Photoluminescence in Zno Phosphor Powders. *J. Appl. Phys.* **1996**, *79*, 7983–7990.

34. Noh, J.; Cho, I.-S.; Lee, S.; Cho, C. M.; Han, H. S.; An, J. S.; Kwak, C. H.; Kim, J. Y.; Jung, H. S.; Lee, J. K.; Hong, K. S. Photoluminescence and Electrical Properties of Epitaxial Al-Doped Zno Transparent Conducting Thin Films. *Phys. Status Solidi A* **2009**, *206*, 2133–2138.

35. Yuk, J. M.; Park, J.; Ercius, P.; Kim, K.; Hellebusch, D. J.; Crommie, M. F.; Lee, J. Y.; Zettl, A.; Alivisatos, A. P. High-Resolution EM of Colloidal Nanocrystal Growth Using Graphene Liquid Cells. *Science* **2012**, *336*, 61–64.

36. De Clercq, A.; Dachraoui, W.; Margeat, O.; Pelzer, K.; Henry, C. R.; Giorgio, S. Growth of Pt-Pd Nanoparticles Studied *in Situ* by HRTEM in a Liquid Cell. *J. Phys. Chem. Lett.* **2014**, *5*, 2126–2130.

37. Hong, S. K.; Hanada, T.; Ko, H. J.; Chen, Y. F.; Yao, T.; Imai, D.; Araki, K.; Shinohara, M.; Saitoh, K.; Terauchi, M. Control of Crystal Polarity in a Wurtzite Crystal: ZnO Films Grown by Plasma-Assisted Molecular-Beam Epitaxy on GaN. *Phys. Rev. B* **2002**, *65*, 115331.

38. Bertoni, G.; Grillo, V.; Brescia, R.; Ke, X. X.; Bals, S.; Catellani, A.; Li, H. B.; Manna, L. Direct Determination of Polarity, Faceting, and Core Location in Colloidal Core/Shell Wurtzite Semiconductor Nanocrystals. *ACS Nano* **2012**, *6*, 6453–6461.

39. Findlay, S. D.; Shibata, N.; Sawada, H.; Okunishi, E.; Kondo, Y.; Yamamoto, T.; Ikuhara, Y. Robust Atomic Resolution Imaging of Light Elements using Scanning Transmission Electron Microscopy. *Appl. Phys. Lett.* **2009**, *95*, 191913.

40. de la Mata, M.; Magen, C.; Gazquez, J.; Utama, M. I.; Heiss, M.; Lopatin, S.; Furtmayr, F.; Fernandez-Rojas, C. J.; Peng, B.; Morante, J. R.; Rurali, R.; Eickhoff, M.; Fontcuberta i Morral, A.; Xiong, Q.; Arbiol, J. Incommensurate van der Waals Epitaxy of Nanowire Arrays: a Case Study with ZnO On Muscovite Mica Substrates. *Nano Lett.* **2012**, *12*, 2579–86.

41. Ghoshal, T.; Kar, S.; Chaudhuri, S. Synthesis and Optical Properties of Nanometer to Micrometer Wide Hexagonal Cones and Columns of ZnO. *J. Cryst. Growth* **2006**, *293*, 438–446.

42. Xuefei, S.; Xiaoqing, Q.; Liping, L.; Guangshe, L. Nature of Catalytic Activities of CoO Nanocrystals in Thermal Decomposition of Ammonium Perchlorate. *Inorg. Chem.* **2008**, *47*, 4146–4152.

43. Crook, S.; Dhariwal, H.; Thornton, G. HREELS Study of the Interaction of Formic Acid with ZnO(1010) and ZnO-(0001)-O. *Surf. Sci.* **1997**, *382*, 19–25.

44. Todorov, I. T.; Smith, W.; Trachenko, K.; Dove, M. T. DL_POLY_3: New Dimensions in Molecular Dynamics Simulations *via* Massive Parallelism. *J. Mater. Chem.* **2006**, *16*, 1911–1918.

45. Humphrey, W.; Dalke, A.; Schulten, K. VMD: Visual Molecular Dynamics. *J. Mol. Graphics Modell.* **1996**, *14*, 33–38.

46. Swope, W. C.; Andersen, H. C.; Berens, P. H.; Wilson, K. R. A Computer Simulation Method for the Calculation of Equilibrium Constants for the Formation of Physical Clusters of Molecules: Application To Small Water Clusters. *J. Chem. Phys.* **1982**, *76*, 637–649.

47. Hestenes, M. R.; Stiefel, E. Methods of Conjugate Gradients for Solving Lineair Systems. *J. Res. Natl. Bur. Stand.* **1952**, *49*, 409–436.

48. Ponder, J. W.; Case, D. A. Force Fields for Protein Simulations. *Adv. Protein Chem.* **2003**, *66*, 27–85.

49. Jakalian, A.; Bush, B. L.; Jack, D. B.; Bayly, C. I. Fast, Efficient Generation of High-Quality Atomic Charges. AM1-BCC Model: I. Method. *J. Comput. Chem.* **2000**, *21*, 132–146.

50. Kulkarni, A. J.; Zhou, M.; Ke, F. J. Orientation and Size Dependence of The Elastic Properties of Zinc Oxide Nanobelts. *Nanotechnology* **2005**, *16*, 2749–2756.

51. Matsui, M.; Akaogi, M. Molecular Dynamics Simulation of The Structural and Physical Properties of The Four Polymorphs of TiO_2. *Mol. Simul.* **1991**, *6*, 239–244.

52. Essmann, U.; Perera, L.; Berkowitz, M. L.; Darden, T.; Lee, H.; Pedersen, L. G. A Smooth Particle Mesh Ewald Method. *J. Chem. Phys.* **1995**, *103*, 8577–8593.

53. Caddeo, C.; Dessi, R.; Melis, C.; Colombo, L.; Mattoni, A. Poly(3-hexylthiophene) Adhesion on Zinc Oxide Nanoneedles. *J. Phys. Chem. C* **2011**, *115*, 16833–16837.

54. Melis, C.; Mattoni, A.; Colombo, L. Atomistic Investigation of Poly(3-hexylthiophene) Adhesion on Nanostructured Titania. *J. Phys. Chem. C* **2010**, *114*, 3401–3406.

55. Melis, C.; Raiteri, P.; Colombo, L.; Mattoni, A. Self-Assembling of Zinc Phthalocyanines on ZnO (101̄0) Surface through Multiple Time Scales. *ACS Nano* **2011**, *5*, 9639–9647.

56. Saba, M. I.; Calzia, V.; Melis, C.; Colombo, L.; Mattoni, A. Atomistic Investigation of the Solid-Liquid Interface between the Crystalline Zinc Oxide Surface and the Liquid Tetrahydrofuran Solvent. *J. Phys. Chem. C* **2012**, *116*, 12644–12648.

57. Saba, M. I.; Mattoni, A. Effect of Thermodynamics and Curvature on the Crystallinity of P3HT Thin Films on ZnO: Insights from Atomistic Simulations. *J. Phys. Chem. C* **2014**, *118*, 4687–4694.

58. Goris, B.; Van den Broek, W.; Batenburg, K. J.; Heidari Mezerji, H.; Bals, S. Electron tomography based on a total variation minimization reconstruction technique. *Ultramicroscopy.* **2011**, *113*, 120–130.